
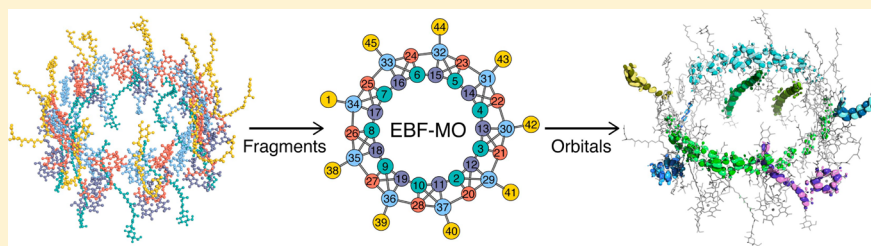


Ground-State Electronic Structure of RC-LH1 and LH2 Pigment Assemblies of Purple Bacteria via the EBF-MO Method

Kushal Shrestha and Elena Jakubikova*

Department of Chemistry, North Carolina State University, Raleigh, North Carolina 27695, United States

 Supporting Information



ABSTRACT: Light-harvesting antennas are protein–pigment complexes that play a crucial role in natural photosynthesis. The antenna complexes absorb light and transfer energy to photosynthetic reaction centers where charge separation occurs. This work focuses on computational studies of the electronic structure of the pigment networks of light-harvesting complex I (LH1), LH1 with the reaction center (RC-LH1), and light-harvesting complex II (LH2) found in purple bacteria. As the pigment networks of LH1, RC-LH1, and LH2 contain thousands of atoms, conventional density functional theory (DFT) and ab initio calculations of these systems are not computationally feasible. Therefore, we utilize DFT in conjunction with the energy-based fragmentation with molecular orbitals method and a semiempirical approach employing the extended Hückel model Hamiltonian to determine the electronic properties of these pigment assemblies. Our calculations provide a deeper understanding of the electronic structure of natural light-harvesting complexes, especially their pigment networks, which could assist in rational design of artificial photosynthetic devices.

INTRODUCTION

Natural photosynthesis is the process by which photosynthetic organisms convert solar energy to chemical energy through a combination of dark and light-driven reactions.¹ It can be divided into four stages, which include light absorption and energy transfer by antenna systems, electron transfer in reaction centers, energy stabilization by secondary processes, and synthesis of stable products.² Studies have shown that the initial light-harvesting process, which consists of light absorption and energy transfer, goes to completion in hundreds of picoseconds with quantum yields greater than 90%.^{3,4} A thorough exposition of this highly efficient photophysical process in plants and bacteria can aid in the design of artificial photosynthetic systems^{5–8} for applications in efficient solar energy conversion devices.

Among the most extensively studied photosynthetic complexes are the antenna systems and bacterial reaction centers of purple bacteria.^{9–14} In the pursuit of a complete understanding of energy transport in bacterial light-harvesting systems, much insight has been gained through the corroboration of experimental results by theoretical models of light absorption and excited-state energy transfer.^{15–21} As such, bacterial antenna systems represent an ideal platform for the testing and development of new computational approaches for the study of natural and artificial light-harvesting systems.

An important feature of photosynthetic complexes is the presence of pigment aggregates that are composed of thousands of atoms. All of the pigments in the aggregate work in concert to achieve light harvesting. Therefore, theoretical models based on quantum mechanics that are capable of treating pigment aggregates in their entirety at the same level of theory are needed to achieve a better understanding of the molecular mechanisms of light harvesting. However, rigorous quantum mechanical simulations of light harvesting in photosynthetic membranes of purple bacteria at the atomic level are not possible with current quantum chemical implementations. This is largely due to the insurmountable computational expense that is tied to the application of many-electron quantum theories to large, biological macromolecular systems consisting of tens of thousands of atoms. Hence, the theoretical treatment of quantum dynamical processes in light-harvesting protein–pigment complexes of purple bacteria^{13,22} have relied on semiempirical and quantum chemically approximate methodologies.²³

Approximate methodologies often employ an effective Hamiltonian that utilizes parameters derived from high-level quantum chemical calculations on smaller subsystems as well as

Received: June 13, 2015

Revised: July 26, 2015

Published: July 28, 2015



spectroscopic measurements to establish experimentally consistent mechanisms for exciton transport in electronically excited protein–pigment complexes.^{21,23,24} The excited-state energy-transfer theories²¹ that are at the heart of such computational modeling are generally based on the theoretical frameworks of Förster theory,^{25–27} Redfield theory,^{16,28} modified Redfield theory,^{29,30} or hierarchy equation of motion approaches.^{31–33}

Accurate electronic structure calculations within the Born–Oppenheimer approximation also play an integral role in theoretical modeling of the excited-state dynamics of large protein–pigment complexes.^{34–40} Specifically, high-level electronic structure methods provide accurate ground-state electron densities,^{41–45} proper characterization and reproduction of vertical Franck–Condon electronic transition energies of pigments,^{37,46–50} and quantum-chemically derived electronic coupling of pigment-localized excited states.^{34–36,38,39} Electronic structure results have become indispensable in the construction of excitonic Hamiltonians,^{23,34,51} and consequently, they play an ever-increasing part in theoretical modeling studies of exciton transport, electronic absorption, and quantum coherence phenomena^{15,52,53} in natural photosynthetic complexes.

While traditional electronic structure calculations have proven their utility in excited-state energy-transfer models specific to light-harvesting complexes,³⁴ they cannot, at the moment, provide a complete description of ground and excited states of entire protein–pigment complexes. Notwithstanding, a holistic quantum chemical account of the electronic structure of protein–pigment complexes could augment current understanding of bacterial light harvesting in yet undiscovered ways.

Nonconventional electronic structure methodologies based on divide-and-conquer approaches or fragmentation methods have already begun to extend quantum-chemical methods to the treatment of large biological macromolecular systems.^{40,54,55} A first step in extending the power of quantum chemistry to entire light-harvesting complexes is the determination of the ground state. Large-scale methodologies like the divide-and-conquer methods,^{56–58} the fragment molecular orbital (FMO) method,^{43,59–61} the FMO with molecular orbitals (FMO-MO)^{62,63} and the FMO-linear combination of MOs (FMO-LCMO)^{64,65} methods, energy-based fragmentation (EBF) methods⁶⁶ (kernel energy method,^{67,68} generalized EBF method,^{69,70} molecular fractionation with conjugate caps method,^{71,72} molecular tailoring approach^{73–75}), the EBF with molecular orbitals (EBF-MO) method,⁷⁶ subsystem density functional theory (DFT),^{77–80} linear scaling methods,^{81–86} and QM/MM⁸⁷ methods are all capable of providing the ground states of large pigment–protein complexes. For example, the FMO method has been used to compute the ground-state density of the photosynthetic reaction center of *Rhodospseudomonas viridis* that consisted of 20 581 atoms and required 164 442 basis functions at the Hartree Fock/6-31G* level of theory.⁴² Similarly, a linear-scaling DFT method successfully obtained the ground-state canonical orbitals of the insulin hexamer that contained 4728 atoms and required 26 790 basis functions.⁴⁴

In this work, we employ the EBF-MO method⁷⁶ in conjunction with DFT to obtain the complete ground-state electronic structure of the pigment assemblies of light-harvesting complexes found in *Rhodospseudomonas* (*Rps.*) *palustris* and *Rps. acidophila*. Specifically, we obtain the ground-state energy and the full set of ground-state Kohn–

Sham orbitals for the pigment assemblies of the reaction center (RC), the core antenna complex (LH1), and the LH1 with RC (RC-LH1) complex of *Rps. palustris*, as well as the peripheral antenna complex (LH2) of *Rps. acidophila* (Figure 1).^{88,89}

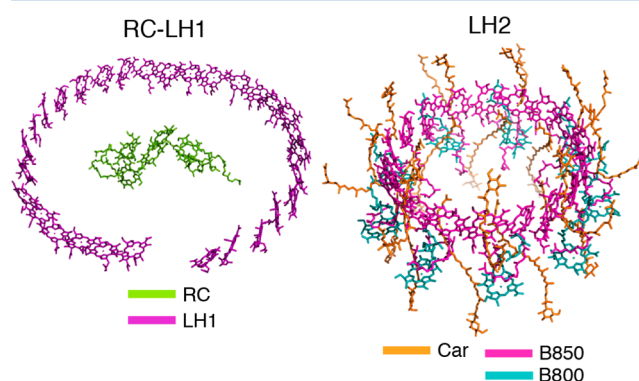


Figure 1. Crystal structures of the RC-LH1 and LH2 pigment assemblies.^{88,89} The RC and LH1 ring were differentiated by color. The carotenoid glucosides (Car), the 18-membered bacteriochlorophyll *a* ring (B850), and the nine-membered bacteriochlorophyll *a* ring (B800) in LH2 are also differentiated.

■ COMPUTATIONAL METHODS

The geometries for RC, LH1, and RC-LH1 pigment assemblies were obtained from the crystal structure data with the Protein Data Bank (PDB) code 1PYH,⁸⁸ while that of the LH2 pigment assembly was obtained from the crystal structure data with PDB code 1NKZ⁸⁹ (see Figure 1). All hydrogens were inserted manually into the structures, resulting in the C–H distances of 1.07 Å. Two structures for the RC were considered, labeled as RC and RC-Hopt. The first one, labeled as RC, corresponds to the crystal structure with manually inserted hydrogens. RC-Hopt structure corresponds to the RC structure with optimized H atoms, in which constrained optimizations of hydrogen atom positions were performed for each pigment of the RC separately. Note that the protein-free pigment assemblies of the two light-harvesting antenna complexes studied herein are referred to in this work as “RC-LH1” and “LH2”.

The ground-state electronic structure of RC, RC-Hopt, LH1, and RC-LH1 was computed using both the B3LYP^{90,91} and CAM-B3LYP⁹² functionals as implemented in the Gaussian 09 (G09) software package.⁹³ The 6-31G* basis set⁹⁴ was chosen for all atoms.

The EBF-MO procedure⁷⁶ was employed at the B3LYP and CAM-B3LYP levels of theory to obtain the ground state for RC, RC-Hopt, LH1, RC-LH1, and LH2. Each system was initially divided into fragments represented by individual chromophores (BChl *a* or Car). A set of overlapping superfragments covering the entire pigment array was then composed. Each superfragment consisted of at most three nearest-neighbor fragments. The systematic fragmentation procedure that resulted in the superfragments of RC, LH1, and LH2 is outlined in the Supporting Information (Figures S1–S3 and Tables S1 and S2). Figure 2a,b illustrates the partitioning of LH2 into fragments, where each fragment is represented by a single pigment. The definition of fragments allows for the determination of the nearest neighbors (Figure 2b), which then determines the superfragments of LH2. The fragmentation scheme of RC-LH1 is a simple sum of the fragmentation schemes of RC and LH1.

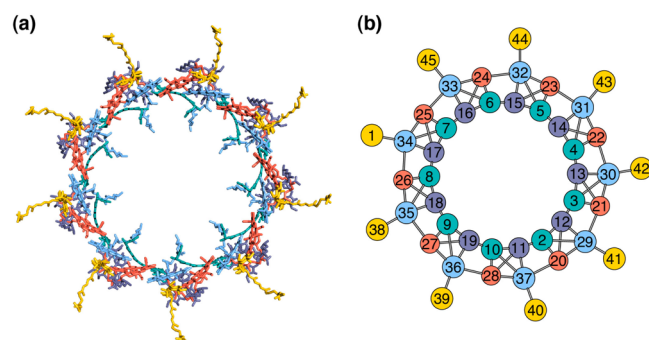


Figure 2. (a) Five types of fragments with unique nearest neighbor environments in the crystal structure of LH2, where each fragment type is differentiated by color. (b) A cartoon representation of LH2 (with the same color scheme as in the crystal structure) that identifies all fragments by numbers. Gray lines connect each fragment to its nearest neighbors. For the full fragmentation scheme of LH2 see also Figure S3 and Table S2.

Single-point energy calculations with a chosen exchange-correlation functional were performed with G09 for all superfragments of a given system. The output from the G09 calculations on the superfragments then served as input for the EBF-MO procedure⁷⁶ to yield EBF-MO ground-state molecular orbitals. The ground-state total energies derived from the EBF-MO orbitals, which are henceforth referred to as the EBF-MO total energy (E_{EBFMO}), for RC, RC-Hopt, LH1, and RC-LH1 were computed by providing the EBF-MO orbitals as initial guesses to the self-consistent field (SCF) procedure in G09 and performing a single SCF step. Additionally, the EBF total energies (E_{EBF}) were computed using superfragment total energies (E_i) and the fragmentation scheme chosen for a given system as

$$E_{\text{EBF}} = \sum_{i=1}^M C_i E_i \quad (1)$$

where C_i are the coefficients determined by the fragmentation scheme, and M is the number of superfragments. The fragmentation schemes for all pigment assemblies along with the coefficients C_i can be found Figures S1–S3 and Tables S1 and S2. Currently, the EBF-MO procedure is implemented using the Python programming language and interfaces exclusively with G09.⁷⁶

In the case of RC, RC-Hopt, LH1, and RC-LH1, the EBF-MO orbitals were provided as initial guesses for the SCF procedure implemented in G09 to obtain the conventional ground-state energy (E_{CONV}) and the corresponding set of Kohn–Sham orbitals. Additionally, ground-state electronic structure for all pigment assemblies was also obtained at the extended Hückel level of theory utilizing the Hoffman parameter set⁹⁵ as implemented in G09. All density of states (DOS) plots were generated utilizing the ground-state orbitals and were obtained by summing Gaussian functions centered at the orbital energy levels. The Gaussian functions had height equal to one with full width at half-maximum of 0.2 eV. Partial DOS (PDOS) plots of the RC and the LH1 subunits of RC-LH1 were obtained with the aid of Mulliken population analysis⁹⁶ of every orbital in RC-LH1. An orbital was deemed to be localized on a given subgroup if 80% or higher of the orbital's population was localized on said subgroup. Partial DOS plots of the Car, B800, and B850 subgroups in LH2 were determined using the same procedure.

The difference density plots between the EBF-MO and conventional total electron densities for RC-LH1 were discretely defined in a volume with dimensions of $66.33 \times 179.40 \times 204.86$ bohr with 166 264 191 evenly spaced spatial points.

RESULTS AND DISCUSSION

Benchmark Calculations. The ground-state energy, orbitals, and orbital energies were computed for RC, RC-Hopt, LH1, and RC-LH1 with the EBF-MO approach, as well as with the conventional DFT implementation. The ground-state electronic structure of LH2 was obtained only with the EBF-MO approach, due to the large size of the system. Note that the ground-state energies of the pigment arrays were obtained in three different ways: (1) as a sum of the superfragment energies (E_{EBF} , eq 1), (2) from a single SCF step utilizing the EBF-MO orbitals (E_{EBFMO}), and (3) from conventional DFT calculations (E_{CONV}). The errors between E_{EBFMO} and E_{CONV} for the benchmark systems were all less than 1 kcal/mol for both levels of theory (Table 1 and Table S3). Interestingly, E_{EBFMO} were upper bounds to the corresponding E_{CONV} at both the B3LYP/6-31G* and CAM-B3LYP/6-31G* levels of theory.

Table 1. EBF-MO/Conventional Total Energy Differences between Total Ground-State Energies of Benchmark Systems at the B3LYP/6-31G* Level of Theory

system	$E_{\text{EBF}} - E_{\text{CONV}}$ (kcal/mol)	$E_{\text{EBFMO}} - E_{\text{CONV}}$ (kcal/mol)
RC	0.128	0.028
RC-Hopt	0.134	0.027
LH1	0.013	0.719
RC-LH1	0.154	0.895

Errors associated with E_{EBF} in Table 1 are different from the errors associated with E_{EBFMO} . The errors in the total energy that arise from the EBF procedure described by eq 1 do not correlate with the size of the system. For example, RC and RC-Hopt have errors that are an order of magnitude higher than that of a much larger system, LH1. Consequently, the majority of the error in E_{EBF} of RC-LH1 is from RC (Table 1). The apparent disparity in the E_{EBF} errors in Table 1 may largely be due to structural differences between RC and LH1, where the pigments in RC are more intertwined than in LH1 (see Figure 1) with possibly more electronic interactions. Hence, the EBF prescription for the total energy shows different levels of accuracy for RC and LH1 not correlated to their system size.

Unlike the E_{EBF} errors, the E_{EBFMO} errors show size dependence. The E_{EBFMO} errors increase by an order of magnitude going from RC/RC-Hopt to LH1. In EBF-MO the accuracy of the total energy hinges on the approximations made when constructing the Fock and overlap matrices. The methodology neglects direct interactions with next-nearest neighbor fragments when constructing relevant matrices.⁷⁶ This directly impacts the accuracy of the occupied orbitals and in turn affects the total energy. The nearest-neighbor fragmentation scheme employed in this work neglects a larger portion of the Fock and overlap matrices as the systems increase in size. Specifically, 34% of matrix elements were neglected in RC and RC-Hopt, while 84% and 87% of matrix elements were neglected for LH1 and RC-LH1, respectively. The errors for E_{EBFMO} in Table 1 correlate with the degree of matrix element

neglect due to the fragmentation scheme for all benchmark systems.

Comparison of the ground-state orbital DOS of RC-LH1 obtained from the EBF-MO and the conventional methods at the B3LYP/6-31G* level of theory shows no apparent differences (Figure 3a). In addition to successfully reproducing

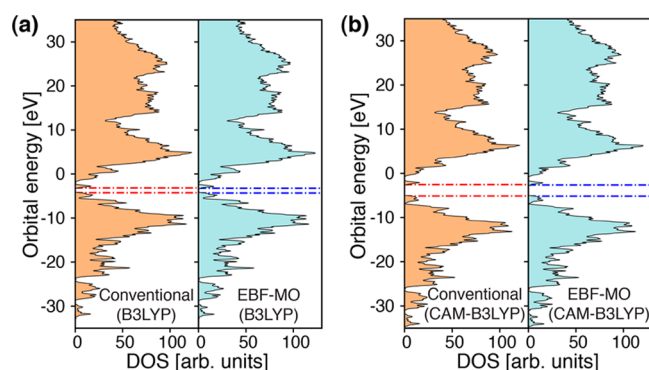


Figure 3. DOS plots for ground-state orbital energies of RC-LH1 (between -35 and 35 eV) from the conventional and the EBF-MO methods at the B3LYP/6-31G* (a) and CAM-B3LYP/6-31G* (b) levels. The HOMO and LUMO orbital energies are both indicated by either red (conventional) or blue (EBF-MO) horizontal dotted-dashed lines.

the B3LYP ground-state orbital DOS of RC-LH1, EBF-MO also provides excellent approximations of the ground-state DOS of RC, RC-Hopt, and LH1 (see Figures S4–S7). The accuracy of the EBF-MO orbital DOS does not diminish for RC, RC-Hopt, LH1, and RC-LH1 when switching to the CAM-B3LYP/6-31G* level of theory (Figure 3b and Figures S4–S7).

The errors with respect to the energy gap between the highest occupied molecular orbital (HOMO) and the lowest unoccupied molecular orbital (LUMO), the HOMO–LUMO gap, that arise from approximations in the EBF-MO method for both B3LYP- and CAM-B3LYP-based benchmark calculations are within ± 0.05 eV (Table 2 and Table S4). Furthermore, the

Table 2. Energy Differences between the EBFMO and Conventional Energies of the HOMO–LUMO Gaps (ΔE_{HL}), the HOMO Orbital Energies (ΔE_{HOMO}), and the LUMO Orbital Energies (ΔE_{LUMO}) of Benchmark Systems^a

system	ΔE_{HL} (eV)	ΔE_{HOMO} (eV)	ΔE_{LUMO} (eV)
RC	−0.012	0.022	0.011
RC-Hopt	−0.008	0.020	0.012
LH1	0.002	−0.052	−0.049
RC-LH1	−0.030	−0.037	−0.067

^aCalculated at the B3LYP/6-31G* level of theory. Results from conventional DFT were subtracted from EBF-MO results.

EBF-MO method accurately reproduces the orbital energies of the HOMO and LUMO. Errors associated specifically with the HOMO energies and with the LUMO energies for both B3LYP- and CAM-B3LYP-based benchmark calculations are within ± 0.08 eV (Table 2 and Table S4 in the Supporting Information).

As the EBF-MO method affords the ground-state orbitals of a given system, it also allows for a direct comparison of the EBF-MO ground-state electron density, $\rho_{\text{EBFMO}}(r)$, with the conventional DFT ground-state electron density, $\rho_{\text{CONV}}(r)$, by

means of a difference density function, $\rho_{\text{EBFMO}}(r) - \rho_{\text{CONV}}(r) = \rho_{\text{DIFF}}(r)$. Integration of $\rho_{\text{DIFF}}(r)$ for RC-LH1 in a sufficiently large volume with discrete spatial points (see Figure S10 in the Supporting Information) results in errors that are less than $\pm 0.0023\%$ of the total electronic charge. Specifically, the error due to the EBF-MO approximation in the total charge for RC-LH1 at the B3LYP/6-31G* level is $\pm 0.30 e$ and is $\pm 0.24 e$ at the CAM-B3LYP/6-31G* level. The largest value of $|\rho_{\text{DIFF}}(r)|$ for RC-LH1 at both levels of theory does not exceed $0.0014 e/\text{bohr}^3$, and values of the discretized $\rho_{\text{DIFF}}(r)$ that are larger than $0.0001 e/\text{bohr}^3$ at both levels of theory are spatially confined to a total volume that is less than $(6.26 \times 6.26 \times 6.26) \text{ bohr}^3$ (see Figure S10 in the Supporting Information).

Comparison with Extended Hückel Theory. Despite the large size of the pigment assemblies in this study, orbitals and orbital energies are readily accessible via the implementation of the extended Hückel theory (EHT). When compared to the HOMO–LUMO gaps of RC-LH1 and LH2 calculated from EBF-MO at the B3LYP/6-31G* level, the corresponding gaps at the EHT level are significantly smaller (Figure 4). This is also

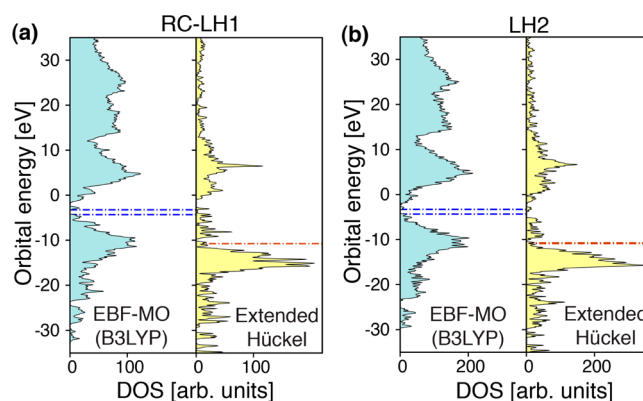


Figure 4. DOS plots for ground-state orbital energies (between -35 and 35 eV) obtained from EHT and the EBF-MO method at the B3LYP/6-31G* level for RC-LH1 and LH2. The HOMO and LUMO orbital energies are both indicated by either red (EHT) or blue (EBF-MO) horizontal dotted-dashed lines.

the case for RC, RC-Hopt, and LH1 (Figures S8 and S9 in the Supporting Information). Table 3 shows the HOMO–LUMO gaps generated by the EBF-MO method and by EHT for all systems in this study and provides quantitative confirmation of the underestimation of these energy gaps by EHT. Furthermore, the overall shapes of the orbital energy DOS plots from EHT are in qualitatively poor agreement with those from EBF-MO (Figures 4, S8, and S9). The Hoffman set of

Table 3. HOMO–LUMO Orbital Energy Gaps^a from EBF-MO and Extended Hückel Theory

system	EBF-MO (CAM-B3LYP) ΔE_{HL} (eV)	EBF-MO (B3LYP) ΔE_{HL} (eV)	EHT ΔE_{HL} (eV)
RC	3.084	1.556	0.448
RC-Hopt	3.122	1.596	0.441
LH1	2.524	1.068	0.002
RC-LH1	2.524	1.068	0.002
LH2 ^b		1.036	0.165

^a ΔE_{HL} refers to the HOMO–LUMO orbital energy gap. ^bThe CAM-B3LYP/6-31G* ground state of LH2 was not obtained in this study.

parameters of EHT does not quantitatively or qualitatively reproduce the orbital energy landscape that results from EBF-MO and by extension from conventional DFT (Figure 3) at the B3LYP/6-31G* and CAM-B3LYP/6-31G* levels of theory for any of the pigment assemblies included in this study. This suggests that a reparameterization of EHT is necessary to provide a qualitatively correct picture of the ground-state electronic structure in these systems. The qualitative accuracy of the EHT orbitals, orbital energies, and extended Hückel Hamiltonian become important in instances where they are incorporated into models of electron dynamics^{97–100} that are often applied in the study of large systems.^{101–106}

Ground-State Electronic Structure of RC-LH1. Figure 5 shows DOS plot for RC-LH1 as well as PDOS plots for the

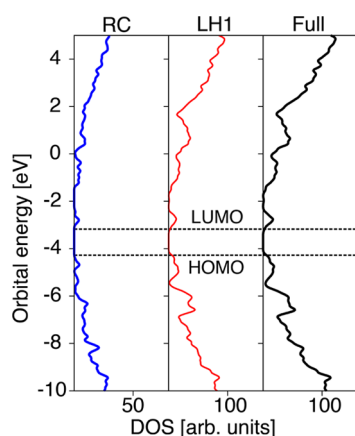


Figure 5. Conventional DFT (B3LYP/6-31G*) orbital energy DOS plots of orbitals localized on two subdivisions; the reaction center (RC), and the 30-membered bacteriochlorophyll ring (LH1); of RC-LH1 are compared to the total DOS. Delocalization of orbitals across both RC and LH1 was not observed. The HOMO and LUMO energies are shown with black dashed lines. Both the HOMO and the LUMO are localized on LH1.

RC-localized and the LH1-localized orbitals in RC-LH1 obtained from conventional DFT calculations. Overall, the RC-localized MOs are interlaced with the LH1-localized MOs across the entire orbital energy spectrum of RC-LH1. A closer examination of the frontier region in the PDOS plots in Figure 5 reveals that the HOMO–LUMO gap is entirely the result of orbitals that are localized on the LH1 ring.

Isosurface plots of the HOMO and LUMO of RC-LH1 in Figure 6 (labeled “H” and “L”) indicate that the two orbitals are localized on two different Bacteriochlorophyll *a* (BChl *a*) pigments in the LH1 ring. The first RC-localized occupied and virtual orbitals in the frontier orbital energy region of RC-LH1 are HOMO–8 and LUMO+6, respectively (see Figure 6). No MOs in the energy region between –5 and –2 eV (HOMO–17 through LUMO+29) exhibit a high degree of spatial delocalization across RC-LH1. Orbital delocalization in this region does not extend beyond three adjacent pigment molecules (see Figure 6 and Figures S12–S16 in the Supporting Information for illustrations of all MOs between –4.8 and –2.6 eV). Furthermore, all orbitals in the frontier region (–4.8 to –2.6 eV) of RC-LH1 can be described as linear combinations of the four frontier orbitals (HOMO–1 through LUMO+1) of the BChl *a* monomer (Figure S11 in the Supporting Information).

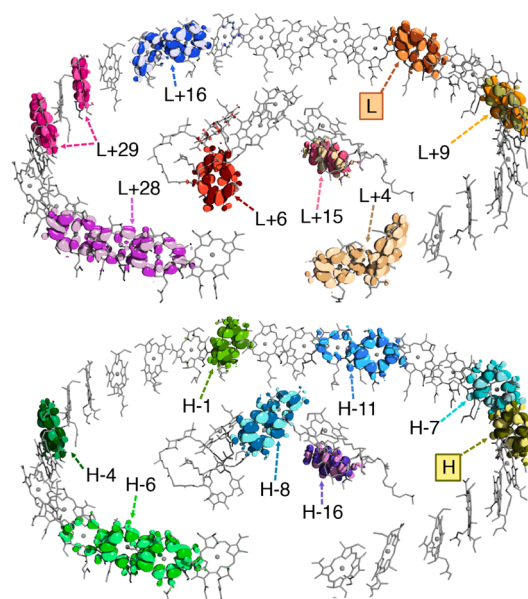


Figure 6. Isosurface plots of some ground-state orbitals (conventional/B3LYP) from HOMO–16 (labeled as H-16) to LUMO+29 (labeled as L+29) of RC-LH1. Orbitals are plotted at an isovalue of $\pm 0.011e/\text{bohr}^3$. The orbitals are differentiated by color scheme and labeling.

Interestingly, all MOs of RC-LH1 pigment array are either fully localized on RC or LH1 subunits, as determined by the Mulliken population analysis. The spatial separation of the RC and the LH1 ring with an edge-to-edge distance of over 18 Å in RC-LH1 is most likely responsible for the lack of orbital mixing across the RC and the LH1 ring.

The above observations for the results from conventional B3LYP calculations on RC-LH1 can readily be extended to results from the EBF-MO method. While orbital energies and orbital ordering are slightly different between conventional B3LYP results and EBF-MO results, the observations on the extent of delocalization of the frontier orbitals are still valid and completely analogous to the EBF-MO results (see juxtaposition of conventional and EBF-MO results in Figures S12–S16 in the Supporting Information). Overall comparisons between the B3LYP and CAM-B3LYP results offer little further insight other than the observation that the CAM-B3LYP functional widens the HOMO–LUMO gap in both conventional and EBF-MO calculations (Table 3 and Figure 3b).

Ground-State Electronic Structure of LH2. The LH2 pigment assembly can be categorized into three distinct pigment groups: the B850 group (18-membered ring of BChl *a* pigments), the B800 group (nine-membered ring of BChl *a* pigments), and the Car group (collection of carotenoid glucoside pigments; see Figure 1). Mulliken population analysis of all LH2 MOs generated using the EBF-MO method indicates that the majority of the orbitals of LH2 share electron density among the three pigment groups. This is in contrast to the RC-LH1 pigment assembly that shows no orbital delocalization between the RC and LH1 pigment groups.

Figure 7 shows PDOS of orbitals strictly localized on each pigment group as well as PDOS of delocalized orbitals constructed using the Mulliken population analysis. Inspection of the PDOS plots in Figure 7 reveals that in the energy region between –15 and 10 eV there is a higher density of group-delocalized orbitals, that is, orbitals with less than 80% of orbital

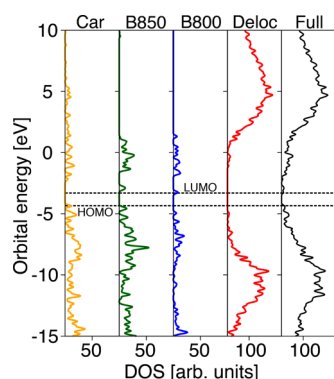


Figure 7. EBF-MO (B3LYP/6-31G*) orbital DOS plot, PDOS plots of orbitals localized on three subdivisions (Car, the 18-membered B850 ring, and the nine-membered B800 ring) of LH2, and PDOS plot for the group-delocalized orbitals (80% of orbital density is not exclusively on any one subdivision: Car, B850, B800). The HOMO and LUMO energies are shown with black dashed lines.

electron density localized on one particular pigment group than group-localized orbitals. This is also the case for the full range of orbital energies (−55 to 90 eV; see Figure S17b in the [Supporting Information](#)).

While group-delocalized orbitals dominate the overall orbital energy spectrum of LH2, group-localized orbitals form the majority in the narrow frontier orbital energy region between −7 and 0 eV. The HOMO and orbitals in the immediate energetic vicinity of the HOMO are localized on Car, while LUMO and orbitals near the LUMO are localized on B800 (Figure 7). Figure 8 illustrates a small set of ground-state orbitals between HOMO−43 and LUMO+62 from the frontier region of LH2. The majority of orbitals localized on Car and B800 groups in the frontier region are further localized on single pigments in those groups, for example, HOMO (labeled “H” in Figure 8) is localized on a single carotenoid glucoside in Car, and LUMO (labeled “L” in Figure 8) is localized on a single BChl *a* pigment in B800. Delocalization of the orbitals in the frontier energy region across both the Car and the B800 groups generally occurs between straight carotenoid glucosides pigments that are in close proximity to the B800 pigments in the lower half of the LH2 ring as demonstrated by HOMO−43 (Figure 8).

The orbital energy landscape near the HOMO–LUMO gap of LH2 generated by EBF-MO at the B3LYP level depicts Car-based orbitals as the highest occupied orbitals followed downhill in energy by B850-based orbitals and then by B800-based orbitals (Figures 7, 8, and S18–S23). These three distinct groups of orbitals all originate from the HOMOs of monomers (see [Supporting Information](#), Figure S11). The unoccupied frontier region begins with B800-based orbitals followed uphill in energy by B850-based orbitals and then by Car-based orbitals (Figures 7, 8, and S18–S23). Analogously, these unoccupied orbitals originate from the monomer lowest unoccupied orbital.

While Car and B800 orbitals in the frontier energy region are localized on one to two pigments, B850-localized orbitals show a high degree of delocalization around the 18-membered pigment ring (see HOMO−12, HOMO−15, and LUMO+16 in Figure 8). Note that a minimal distance of ~4 Å spatially separates individual pigments in the B850 ring. The close proximity of the pigments may explain the extensive π delocalization in the B850 frontier orbitals despite the lack of interpigment covalent bonds.

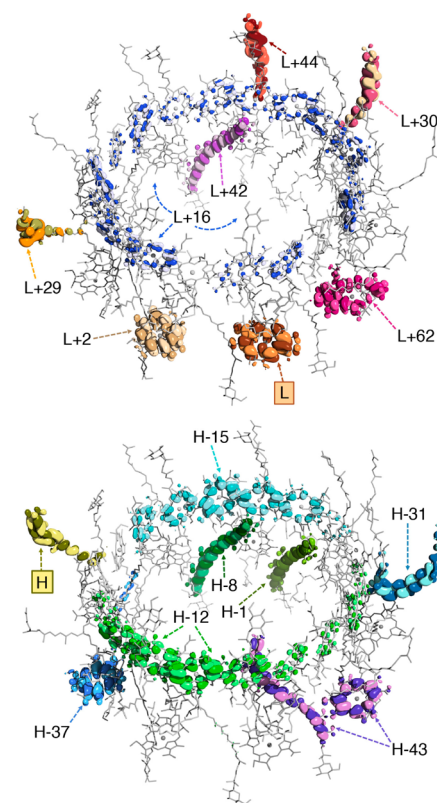


Figure 8. Isosurface plots of several ground-state orbitals (EBF-MO/B3LYP) from HOMO−43 (labeled as H−43) to LUMO+62 (labeled as L+62) of LH2. Orbitals are plotted at an isovalue of $\pm 0.011 e/\text{bohr}^3$. The orbitals are differentiated by color scheme and labeling.

The delocalized occupied and unoccupied orbitals confined to the B850 ring can be described as linear combinations of monomer BChl *a* frontier orbitals (see monomer orbitals in Figure S11). For instance, the 18 occupied, B850-based orbitals between −4.47 and −4.68 eV result from linear combinations of the HOMOs of 18 monomer BChl *a* molecules. These orbitals exhibit a high degree of delocalization over the entire B850 ring and comprise HOMO−12 through HOMO−29 of LH2 (Figures S21–S23). Similarly, LUMO+9 through LUMO+26 correspond to linear combinations of the monomer pigments’ LUMOs and are highly delocalized over the entire B850 ring (Figures S18 and S19). In this fashion, the B850 ring contains four groups of 18 delocalized orbitals in the frontier energy region that can be divided into two occupied groups and two unoccupied groups originating from mixing between the four frontier orbitals of BChl *a*. More generally, all orbitals of LH2 between −2.0 and −5.0 eV originate from the four frontier orbitals of BChl *a* and carotenoid glucoside. The level of delocalization observed for orbitals between −2.0 and −5.0 eV of LH2 can be viewed as a manifestation of interpigment interactions. Therefore, the level delocalization of the orbitals in a certain energy range (readily provided by the EBF-MO method) can serve as a qualitative handle for the amount of interpigment interactions for a group of pigments in an assembly.

Overall, our application of the EBF-MO method demonstrates that a set of ground-state canonical orbitals is obtainable for systems with thousands of atoms at a relatively high level of theory. Moreover, results for RC, LH1, and RC-LH1 clearly indicate that the EBF-MO orbitals can serve as an excellent

initial guess for the SCF procedure. Linear scaling methodologies where convergence in the SCF procedure is sensitive to the initial guess for orbitals^{44,107} could benefit from the incorporation of the EBF-MO orbitals as the initial guess.

Note that the ground-state electronic structure of RC-LH1 and LH2 was obtained without the native protein environment of these light-harvesting protein–pigment complexes. Inclusion of the protein environment is expected to perturb the ground-state electronic structure.^{108–110} Nevertheless, the above results for the two assemblies obtained via the EBF-MO method provide both a qualitative and quantitative assessment of electronic interactions between constituent pigments at a relatively high level of theory. Although this is not addressed in this work, the added complication of electronic interactions with protein residues can be readily tackled by the EBF-MO method for a better description of the ground-state electronic structure.

Timing Data. Finally, timing data for EBF-MO calculations are presented in Table 4. The data include system sizes such as

Table 4. Timing Data and System Sizes for EBF-MO and Conventional Calculations at the B3LYP/6-31G* Level of Theory

	RC	LH1	RC-LH1	LH2
basis set size	6428	22 140	28 568	44 536
no. atoms	842	2550	3392	5906
no. electrons	2932	10 260	13 192	20 306
no. SF's	7	55	62	315
SF SPE ^a (h)	1.4	0.7	1.4	4.5
matrix build ^b (h)	0.1	2.5	6.6	181.4
roothaan ^b (h)	0.6	19.3	40.0	198.2
output file ^b (h)	0.3	2.5	4.3	20.6
EBF-MO total (h)	2.4	24.9	52.3	404.6
conv. SCF ^c (h)	35.6	84.1	211.3	
no. conv. SCF cycles	10	11	13	

^aSF SPE represents the wall time for the largest superfragment using 16 CPU cores and 60 GB of memory. ^b62 CPU cores with 250 GB of memory were utilized for these calculations. ^cEBF-MO orbitals were used as initial guesses for the conventional SCF procedure (number of cycles until convergence shown) calculations which utilized 16 CPU cores (500 GB of memory).

number of atoms, electrons, and superfragments. Wall times for both EBF-MO and conventional calculations of RC, LH1, RC-LH1, and LH2 at the B3LYP/6-31G* level of theory are also shown in Table 4, labeled as “EBF-MO total” and “Conv. SCF”, respectively. The number of CPU cores (1.0 GHz AMD Opteron) was kept constant at 62, with 250 GB of memory available for the EBF-MO procedure performed independently of G09.

The total computation time for each system in Table 4 was partitioned into the four distinct steps of the EBF-MO implementation, labeled as “SF SPE” (superfragment single point energy), “Matrix Build”, “Roothaan”, and “Output File”. The first step, “SF SPE”, requires obtaining an SCF solution for each of the superfragments. All single-point calculations for superfragments are independent of each other and can thus be performed in parallel. Therefore, only the total time taken for the SCF solution of the largest superfragment is reported in Table 4. In this work, each superfragment single-point energy calculation utilized 16 cores (1.8 GHz Intel Xeon) and 60 GB of memory.

Note that, of the four steps in our implementation of the EBF-MO procedure, only the first three steps take advantage of parallel computing architectures, while the last step (the creation of an output file as a g09 formatted checkpoint file, labeled as Output File) is performed sequentially using a single CPU core. The other two parallelized steps are the following: (1) building of the Fock and overlap matrices out of the Fock and overlap matrices of the superfragment (labeled as matrix build) and (2) obtaining the solution to the resulting Roothaan equations¹¹¹ with matrices constructed from a given fragmentation scheme (labeled as Roothaan).⁷⁶ As a result of sequential execution, the total time to create the output file increases rapidly with the system size (Table 4). Finally, a conventional DFT solution for the LH2 system using the EBF-MO orbitals as an initial guess was inaccessible due to the large size of this system (44 536 basis functions and 5906 atoms).

The timing data in Table 4 indicates that as the system size increases, the construction of relevant matrices and the evaluation of the Roothaan equations become bottlenecks with respect to the computation time for the EBF-MO method. Although matrix construction in the current implementation is highly parallel, the absence of direct integration to available quantum chemistry software packages forces heavy preprocessing of printed output. Therefore, the matrix construction step will demonstrate significant efficiency gains when measures are taken to bypass file-oriented preprocessing. Computation time for the evaluation of the Roothaan equation can also be greatly reduced by incorporating scalable algorithms for matrix operations.

CONCLUSIONS

The EBF-MO method at the B3LYP/6-31G* and CAM-B3LYP/6-31G* levels of theory has been applied to ground-state calculations of very large pigment assemblies of purple bacteria: RC (842 atoms), LH1 (2,550 atoms), and RC-LH1 (3,392 atoms). Comparison with ground-state electronic structure obtained from the benchmark calculations on these systems shows that EBF-MO accurately reproduces the total energies, orbital energies, as well as orbital shapes of bacterial pigment assemblies at these levels of theory. Additionally, it was shown that EHT with the Hoffman parameter set is unable to accurately approximate the results obtained by the conventional and EBF-MO DFT methods. Therefore, a reparameterization of the EH Hamiltonian is necessary to apply this approach to calculations of the pigment assemblies in purple bacteria.

The EBF-MO method was also applied to electronic structure calculations of the LH2 pigment assembly composed of 5906 atoms. The close proximity of BChl *a* pigments in the B850 ring of LH2 facilitates extensive π -delocalization over the entire ring despite the absence of covalent bonds between the pigments. This is in contrast to the RC-LH1 system, in which MOs are delocalized over at most three neighboring BChl *a* pigments. The extent of MO delocalization in RC-LH1 and LH2 might have direct consequences for the type of excitons that are formed upon interaction of these systems with light.

Overall, this work illustrates that the EBF-MO approach can provide a holistic and accurate description of the electronic structure of natural pigment complexes at the DFT level of theory.

■ ASSOCIATED CONTENT

■ Supporting Information

The Supporting Information is available free of charge on the ACS Publications website at DOI: 10.1021/acs.jpca.5b05644.

Figures and tables of fragmentation schemes for RC, LH1, RC-LH1, and LH2, figures of CAM-B3LYP and B3LYP DOS comparisons between conventional and EBF-MO ground states, tables of CAM-B3LYP EBF-MO error values, figures of DOS comparisons between CAM-B3LYP and EHT, figures of EBF-MO/conventional density difference plots, figures of MO's of monomer pigments, RC-LH1, and LH2 in the frontier energy region. (PDF)

■ AUTHOR INFORMATION

Corresponding Author

*E-mail: ejakubi@ncsu.edu.

Notes

The authors declare no competing financial interest.

■ ACKNOWLEDGMENTS

This work was supported by the Dept. of Chemistry at North Carolina State Univ. (NCSSU) and used the computing resources of the High Performance Computing Center at NCSSU.

■ REFERENCES

- (1) Rabinowitch, E.; Govindjee, G. *Photosynthesis*; John Wiley & Sons, Inc.: New York, 1969.
- (2) Blankenship, R. E. *Molecular Mechanisms of Photosynthesis*; Blackwell Science Ltd: Great Britain, 2002.
- (3) Borisov, A. Y.; Freiberg, A. M.; Godik, V. I.; Rebane, K. K.; Timpmann, K. E. Kinetics of Picosecond Bacteriochlorophyll Luminescence in Vivo as a Function of the Reaction Center State. *Biochim. Biophys. Acta, Bioenerg.* **1985**, *807*, 221–229.
- (4) Sundström, V.; van Grondelle, R.; Bergström, H.; Åkesson, E.; Gillbro, T. Excitation-Energy Transport in the Bacteriochlorophyll Antenna Systems of Rhodospirillum Rubrum and Rhodobacter Sphaeroides, Studied by Low-Intensity Picosecond Absorption Spectroscopy. *Biochim. Biophys. Acta, Bioenerg.* **1986**, *851*, 431–446.
- (5) Odobel, F.; Pellegrin, Y.; Warnan, J. Bio-Inspired Artificial Light-Harvesting Antennas for Enhancement of Solar Energy Capture in Dye-Sensitized Solar Cells. *Energy Environ. Sci.* **2013**, *6*, 2041–2052.
- (6) Eremin, V. V.; Belov, A. S. Structure and Properties of Photosynthetic Antennas: Natural and Artificial Complexes. *Russ. Chem. Rev.* **2012**, *81*, 662.
- (7) Gust, D.; Moore, T. A.; Moore, A. L. Molecular Mimicry of Photosynthetic Energy and Electron Transfer. *Acc. Chem. Res.* **1993**, *26*, 198–205.
- (8) Balaban, T. S. Tailoring Porphyrins and Chlorins for Self-Assembly in Biomimetic Artificial Antenna Systems. *Acc. Chem. Res.* **2005**, *38*, 612–623.
- (9) van Grondelle, R.; Novoderezhkin, V. I. Energy Transfer in Photosynthesis: Experimental Insights and Quantitative Models. *Phys. Chem. Chem. Phys.* **2006**, *8*, 793–807.
- (10) Olson, T. L.; Williams, J. C.; Allen, J. P. The Three-Dimensional Structures of Bacterial Reaction Centers. *Photosynth. Res.* **2014**, *120*, 87–98.
- (11) Pullerits, T.; Sundström, V. Photosynthetic Light-Harvesting Pigment–Protein Complexes: Toward Understanding How and Why. *Acc. Chem. Res.* **1996**, *29*, 381–389.
- (12) Cogdell, R. J.; Southall, J.; Gardiner, A. T.; Law, C. J.; Gall, A.; Roszak, A. W.; Isaacs, N. W. How Purple Photosynthetic Bacteria Harvest Solar Energy. *C. R. Chim.* **2006**, *9*, 201–206.
- (13) Cogdell, R. J.; Gall, A.; Kohler, J. The Architecture and Function of the Light-Harvesting Apparatus of Purple Bacteria: From Single Molecules to in Vivo Membranes. *Q. Rev. Biophys.* **2006**, *39*, 227–324.
- (14) Scholes, G. D.; Fleming, G. R.; Olaya-Castro, A.; van Grondelle, R. Lessons from Nature About Solar Light Harvesting. *Nat. Chem.* **2011**, *3*, 763–774.
- (15) Ishizaki, A.; Fleming, G. R. Quantum Coherence in Photosynthetic Light Harvesting. *Annu. Rev. Condens. Matter Phys.* **2012**, *3*, 333–361.
- (16) Renger, T.; May, V.; Kühn, O. Ultrafast Excitation Energy Transfer Dynamics in Photosynthetic Pigment–Protein Complexes. *Phys. Rep.* **2001**, *343*, 137–254.
- (17) Linnanto, J. M.; Korppi-Tommola, J. E. I. Modelling Excitonic Energy Transfer in the Photosynthetic Unit of Purple Bacteria. *Chem. Phys.* **2009**, *357*, 171–180.
- (18) Kühn, O.; Sundström, V. Energy Transfer and Relaxation Dynamics in Light-Harvesting Antenna Complexes of Photosynthetic Bacteria. *J. Phys. Chem. B* **1997**, *101*, 3432–3440.
- (19) Cory, M. G.; Zerner, M. C.; Hu, X.; Schulten, K. Electronic Excitations in Aggregates of Bacteriochlorophylls. *J. Phys. Chem. B* **1998**, *102*, 7640–7650.
- (20) Barter, L. M. C.; Klug, D. R. A Unified Picture of Energy and Electron Transfer in Primary Photosynthesis. *Chem. Phys.* **2005**, *319*, 308–315.
- (21) Renger, T. Theory of Excitation Energy Transfer: From Structure to Function. *Photosynth. Res.* **2009**, *102*, 471–485.
- (22) Green, B. R.; Anderson, J. M.; Parson, W. W. Photosynthetic Membranes and Their Light-Harvesting Antennas. In *Light-Harvesting Antennas in Photosynthesis*; Green, B. R., Parson, W. W., Eds.; Advances in Photosynthesis and Respiration; Kluwer Academic Publishers: Boston, MA, 2003; pp 1–28.
- (23) Pachon, L. A.; Brumer, P. Computational Methodologies and Physical Insights into Electronic Energy Transfer in Photosynthetic Light-Harvesting Complexes. *Phys. Chem. Chem. Phys.* **2012**, *14*, 10094–10108.
- (24) You, Z.-Q.; Hsu, C.-P. Theory and Calculation for the Electronic Coupling in Excitation Energy Transfer. *Int. J. Quantum Chem.* **2014**, *114*, 102–115.
- (25) Förster, T. Zwischenmolekulare Energiewanderung Und Fluoreszenz. *Ann. Phys.* **1948**, *437*, 55–75.
- (26) Šener, M.; Strümpfer, J.; Hsin, J.; Chandler, D.; Scheuring, S.; Hunter, C. N.; Schulten, K. Förster Energy Transfer Theory as Reflected in the Structures of Photosynthetic Light-Harvesting Systems. *ChemPhysChem* **2011**, *12*, 518–531.
- (27) Mukai, K.; Abe, S.; Sumi, H. Theory of Rapid Excitation-Energy Transfer from B800 to Optically-Forbidden Exciton States of B850 in the Antenna System LH2 of Photosynthetic Purple Bacteria. *J. Phys. Chem. B* **1999**, *103*, 6096–6102.
- (28) Redfield, A. G. On the Theory of Relaxation Processes. *IBM J. Res. Dev.* **1957**, *1*, 19–31.
- (29) Renger, T.; Marcus, R. A. On the Relation of Protein Dynamics and Exciton Relaxation in Pigment–Protein Complexes: An Estimation of the Spectral Density and a Theory for the Calculation of Optical Spectra. *J. Chem. Phys.* **2002**, *116*, 9997–10019.
- (30) Yang, M.; Fleming, G. R. Influence of Phonons on Exciton Transfer Dynamics: Comparison of the Redfield, Förster, and Modified Redfield Equations. *Chem. Phys.* **2002**, *275*, 355–372.
- (31) Ishizaki, A.; Fleming, G. R. Unified Treatment of Quantum Coherent and Incoherent Hopping Dynamics in Electronic Energy Transfer: Reduced Hierarchy Equation Approach. *J. Chem. Phys.* **2009**, *130*, 234111.
- (32) Strümpfer, J.; Schulten, K. Open Quantum Dynamics Calculations with the Hierarchy Equations of Motion on Parallel Computers. *J. Chem. Theory Comput.* **2012**, *8*, 2808–2816.
- (33) Strümpfer, J.; Schulten, K. Excited State Dynamics in Photosynthetic Reaction Center and Light Harvesting Complex 1. *J. Chem. Phys.* **2012**, *137*, 065101.

- (34) König, C.; Neugebauer, J. Quantum Chemical Description of Absorption Properties and Excited-State Processes in Photosynthetic Systems. *ChemPhysChem* **2012**, *13*, 386–425.
- (35) Scholes, G. D.; Gould, I. R.; Cogdell, R. J.; Fleming, G. R. Ab Initio Molecular Orbital Calculations of Electronic Couplings in the LH2 Bacterial Light-Harvesting Complex of Rps. Acidophila. *J. Phys. Chem. B* **1999**, *103*, 2543–2553.
- (36) Neugebauer, J. Subsystem-Based Theoretical Spectroscopy of Biomolecules and Biomolecular Assemblies. *ChemPhysChem* **2009**, *10*, 3148–3173.
- (37) König, C.; Neugebauer, J. First-Principles Calculation of Electronic Spectra of Light-Harvesting Complex Ii. *Phys. Chem. Chem. Phys.* **2011**, *13*, 10475–10490.
- (38) König, C.; Neugebauer, J. Exciton Coupling Mechanisms Analyzed with Subsystem TDDFT: Direct Vs Pseudo Exchange Effects. *J. Phys. Chem. B* **2013**, *117*, 3480–3487.
- (39) König, C.; Schlüter, N.; Neugebauer, J. Direct Determination of Exciton Couplings from Subsystem Time-Dependent Density-Functional Theory within the Tamm-Dancoff Approximation. *J. Chem. Phys.* **2013**, *138*, 034104–034115.
- (40) Merz, K. M. Using Quantum Mechanical Approaches to Study Biological Systems. *Acc. Chem. Res.* **2014**, *47*, 2804–2811.
- (41) Jacob, C. R.; Visscher, L. A Subsystem Density-Functional Theory Approach for the Quantum Chemical Treatment of Proteins. *J. Chem. Phys.* **2008**, *128*, 155102.
- (42) Ikegami, T.; Ishida, T.; Fedorov, D. G.; Kitaura, K.; Inadomi, Y.; Umeda, H.; Yokokawa, M.; Sekiguchi, S. Full Electron Calculation Beyond 20 000 Atoms: Ground Electronic State of Photosynthetic Proteins. In *Supercomputing, 2005*, Proceedings of the ACM/IEEE SC 2005 Conference, Seattle, WA, Nov 12–18, 2005; IEEE: New York, 2005.
- (43) Tanaka, S.; Mochizuki, Y.; Komeiji, Y.; Okiyama, Y.; Fukuzawa, K. Electron-Correlated Fragment-Molecular-Orbital Calculations for Biomolecular and Nano Systems. *Phys. Chem. Chem. Phys.* **2014**, *16*, 10310–10344.
- (44) Inaba, T.; Tsunekawa, N.; Hirano, T.; Yoshihiro, T.; Kashiwagi, H.; Sato, F. Density Functional Calculation of the Electronic Structure on Insulin Hexamer. *Chem. Phys. Lett.* **2007**, *434*, 331–335.
- (45) Li, S.; Li, W.; Ma, J. Generalized Energy-Based Fragmentation Approach and Its Applications to Macromolecules and Molecular Aggregates. *Acc. Chem. Res.* **2014**, *47*, 2712–2720.
- (46) Yoshikawa, T.; Kobayashi, M.; Fujii, A.; Nakai, H. Novel Approach to Excited-State Calculations of Large Molecules Based on Divide-and-Conquer Method: Application to Photoactive Yellow Protein. *J. Phys. Chem. B* **2013**, *117*, 5565–5573.
- (47) Ren, Y.; Cheng, L.; Wan, J.; Li, Y.; Liu, J.; Yang, G.; Zhang, L.; Yang, S. A Theoretical Study of Electronic Excited States of Photosynthetic Reaction Center in Rhodospseudomonas Viridis. *Sci. China, Ser. B: Chem.* **2006**, *49*, 88–96.
- (48) He, Z.; Sundström, V.; Pullerits, T. Excited States of Carotenoid in LH2: An Ab Initio Study. *Chem. Phys. Lett.* **2001**, *334*, 159–167.
- (49) Linnanto, J.; Freiberg, A.; Korppi-Tommola, J. Quantum Chemical Simulations of Excited-State Absorption Spectra of Photosynthetic Bacterial Reaction Center and Antenna Complexes. *J. Phys. Chem. B* **2011**, *115*, 5536–5544.
- (50) Dreuw, A.; Harbach, P. H. P.; Mewes, J. M.; Wormit, M. Quantum Chemical Excited State Calculations on Pigment-Protein Complexes Require Thorough Geometry Re-Optimization of Experimental Crystal Structures. *Theor. Chem. Acc.* **2010**, *125*, 419–426.
- (51) Olbrich, C.; Liebers, J.; Kleinekathöfer, U. Modeling of Light-Harvesting in Purple Bacteria Using a Time-Dependent Hamiltonian Approach. *Phys. Status Solidi B* **2011**, *248*, 393–398.
- (52) Chin, A. W.; Huelga, S. F.; Plenio, M. B. Coherence and Decoherence in Biological Systems: Principles of Noise-Assisted Transport and the Origin of Long-Lived Coherences. *Philos. Trans. R. Soc., A* **2012**, *370*, 3638–3657.
- (53) Tiersch, M.; Popescu, S.; Briegel, H. J. A Critical View on Transport and Entanglement in Models of Photosynthesis. *Philos. Trans. R. Soc., A* **2012**, *370*, 3771–3786.
- (54) Akimov, A. V.; Prezhdo, O. V. Large-Scale Computations in Chemistry: A Bird's Eye View of a Vibrant Field. *Chem. Rev. (Washington, DC, U. S.)* **2015**, *115*, 5797.
- (55) Gordon, M. S.; Fedorov, D. G.; Pruitt, S. R.; Slipchenko, L. V. Fragmentation Methods: A Route to Accurate Calculations on Large Systems. *Chem. Rev.* **2012**, *112*, 632–672.
- (56) Yang, W.; Lee, T.-S. A Density-Matrix Divide-and-Conquer Approach for Electronic Structure Calculations of Large Molecules. *J. Chem. Phys.* **1995**, *103*, 5674–5678.
- (57) He, X.; Merz, K. M. Divide and Conquer Hartree-Fock Calculations on Proteins. *J. Chem. Theory Comput.* **2010**, *6*, 405–411.
- (58) Kobayashi, M.; Nakai, H. How Does It Become Possible to Treat Delocalized and/or Open-Shell Systems in Fragmentation-Based Linear-Scaling Electronic Structure Calculations? The Case of the Divide-and-Conquer Method. *Phys. Chem. Chem. Phys.* **2012**, *14*, 7629–7639.
- (59) Kitaura, K.; Ikeo, E.; Asada, T.; Nakano, T.; Uebayasi, M. Fragment Molecular Orbital Method: An Approximate Computational Method for Large Molecules. *Chem. Phys. Lett.* **1999**, *313*, 701–706.
- (60) Fedorov, D. G.; Kitaura, K. Extending the Power of Quantum Chemistry to Large Systems with the Fragment Molecular Orbital Method. *J. Phys. Chem. A* **2007**, *111*, 6904–6914.
- (61) Fedorov, D. G.; Nagata, T.; Kitaura, K. Exploring Chemistry with the Fragment Molecular Orbital Method. *Phys. Chem. Chem. Phys.* **2012**, *14*, 7562–7577.
- (62) Inadomi, Y.; Nakano, T.; Kitaura, K.; Nagashima, U. Definition of Molecular Orbitals in Fragment Molecular Orbital Method. *Chem. Phys. Lett.* **2002**, *364*, 139–143.
- (63) Umeda, H.; Inadomi, Y.; Watanabe, T.; Yagi, T.; Ishimoto, T.; Ikegami, T.; Tadano, H.; Sakurai, T.; Nagashima, U. Parallel Fock Matrix Construction with Distributed Shared Memory Model for the FMO-MO Method. *J. Comput. Chem.* **2010**, *31*, 2381–2388.
- (64) Tsuneyuki, S.; Kobori, T.; Akagi, K.; Sodeyama, K.; Terakura, K.; Fukuyama, H. Molecular Orbital Calculation of Biomolecules with Fragment Molecular Orbitals. *Chem. Phys. Lett.* **2009**, *476*, 104–108.
- (65) Nishioka, H.; Ando, K. Electronic Coupling Calculation and Pathway Analysis of Electron Transfer Reaction Using Ab Initio Fragment-Based Method. I. FMO-LCMO Approach. *J. Chem. Phys.* **2011**, *134*, 204109.
- (66) Collins, M. A.; Bettens, R. P. A. Energy-Based Molecular Fragmentation Methods. *Chem. Rev. (Washington, DC, U. S.)* **2015**, *115*, 5607.
- (67) Huang, L.; Massa, L.; Karle, J. Kernel Energy Method Illustrated with Peptides. *Int. J. Quantum Chem.* **2005**, *103*, 808–817.
- (68) Huang, L.; Massa, L.; Karle, J. The Kernel Energy Method of Quantum Mechanical Approximation Carried to Fourth-Order Terms. *Proc. Natl. Acad. Sci. U. S. A.* **2008**, *105*, 1849–1854.
- (69) Li, W.; Li, S.; Jiang, Y. Generalized Energy-Based Fragmentation Approach for Computing the Ground-State Energies and Properties of Large Molecules. *J. Phys. Chem. A* **2007**, *111*, 2193–2199.
- (70) Hua, S.; Li, W.; Li, S. The Generalized Energy-Based Fragmentation Approach with an Improved Fragmentation Scheme: Benchmark Results and Illustrative Applications. *ChemPhysChem* **2013**, *14*, 108–115.
- (71) Li, S.; Li, W.; Fang, T. An Efficient Fragment-Based Approach for Predicting the Ground-State Energies and Structures of Large Molecules. *J. Am. Chem. Soc.* **2005**, *127*, 7215–7226.
- (72) Brinkmann, L.; Heifets, E.; Kantorovich, L. Density Functional Calculations of Extended, Periodic Systems Using Coulomb Corrected Molecular Fractionation with Conjugated Caps Method (Cc-Mfcc). *Phys. Chem. Chem. Phys.* **2014**, *16*, 21252–21270.
- (73) Ganesh, V.; Dongare, R. K.; Balanarayan, P.; Gadre, S. R. Molecular Tailoring Approach for Geometry Optimization of Large Molecules: Energy Evaluation and Parallelization Strategies. *J. Chem. Phys.* **2006**, *125*, 104109.

- (74) Yeole, S. D.; Gadre, S. R. On the Applicability of Fragmentation Methods to Conjugated π Systems within Density Functional Framework. *J. Chem. Phys.* **2010**, *132*, 094102.
- (75) Sahu, N.; Gadre, S. R. Molecular Tailoring Approach: A Route for Ab Initio Treatment of Large Clusters. *Acc. Chem. Res.* **2014**, *47*, 2739–2747.
- (76) Tsuchiya, T.; Shrestha, K.; Jakubikova, E. Orbital Analysis and Excited-State Calculations in an Energy-Based Fragmentation Method. *J. Chem. Theory Comput.* **2013**, *9*, 3350–3363.
- (77) Neugebauer, J. Couplings between Electronic Transitions in a Subsystem Formulation of Time-Dependent Density Functional Theory. *J. Chem. Phys.* **2007**, *126*, 134116.
- (78) Solovyeva, A.; Pavanello, M.; Neugebauer, J. Spin Densities from Subsystem Density-Functional Theory: Assessment and Application to a Photosynthetic Reaction Center Complex Model. *J. Chem. Phys.* **2012**, *136*, 194104.
- (79) Jacob, C. R.; Neugebauer, J. Subsystem Density-Functional Theory. *Wiley Interdiscip. Rev.: Comput. Mol. Sci.* **2014**, *4*, 325–362.
- (80) Solovyeva, A.; Pavanello, M.; Neugebauer, J. Describing Long-Range Charge-Separation Processes with Subsystem Density-Functional Theory. *J. Chem. Phys.* **2014**, *140*, 164103.
- (81) Galli, G. Linear Scaling Methods for Electronic Structure Calculations and Quantum Molecular Dynamics Simulations. *Curr. Opin. Solid State Mater. Sci.* **1996**, *1*, 864–874.
- (82) Wu, S. Y.; Jayanthi, C. S. Order-N Methodologies and Their Applications. *Phys. Rep.* **2002**, *358*, 1–74.
- (83) Rudberg, E.; Rubensson, E. H.; Salek, P. Kohn–Sham Density Functional Theory Electronic Structure Calculations with Linearly Scaling Computational Time and Memory Usage. *J. Chem. Theory Comput.* **2011**, *7*, 340–350.
- (84) Bowler, D. R.; Miyazaki, T. $O(N)$ Methods in Electronic Structure Calculations. *Rep. Prog. Phys.* **2012**, *75*, 036503.
- (85) Chow, E.; Liu, X.; Smelyanskiy, M.; Hammond, J. R. Parallel Scalability of Hartree–Fock Calculations. *J. Chem. Phys.* **2015**, *142*, 104103.
- (86) Yoshihiro, T.; Sato, F.; Kashiwagi, H. Distributed Parallel Processing by Using the Object-Oriented Technology in ProteinDF Program for All-Electron Calculations on Proteins. *Chem. Phys. Lett.* **2001**, *346*, 313–321.
- (87) Senn, H. M.; Thiel, W. QM/MM Methods for Biomolecular Systems. *Angew. Chem., Int. Ed.* **2009**, *48*, 1198–1229.
- (88) Law, C. J.; Howard, T. D.; Southall, J.; Gardiner, A. T.; Roszak, A. W.; Isaacs, N. W.; Cogdell, R. J. Crystal Structure of the RC-LH1 Core Complex from Rhodospseudomonas Palustris. *Science* **2003**, *302*, 1969–1972.
- (89) Papiz, M. Z.; Prince, S. M.; Howard, T.; Cogdell, R. J.; Isaacs, N. W. The Structure and Thermal Motion of the B800–850 LH2 Complex from Rps. Acidophila at 2.0 Å Resolution and 100 K: New Structural Features and Functionally Relevant Motions. *J. Mol. Biol.* **2003**, *326*, 1523–1538.
- (90) Becke, A. D. Density-Functional Thermochemistry. III. The Role of Exact Exchange. *J. Chem. Phys.* **1993**, *98*, 5648–5652.
- (91) Hess, B. A.; Schaad, L. J.; Carsky, P.; Zahradnik, R. Ab Initio Calculations of Vibrational Spectra and Their Use in the Identification of Unusual Molecules. *Chem. Rev. (Washington, DC, U. S.)* **1986**, *86*, 709–730.
- (92) Yanai, T.; Tew, D. P.; Handy, N. C. A New Hybrid Exchange–Correlation Functional Using the Coulomb-Attenuating Method (Cam-B3lyp). *Chem. Phys. Lett.* **2004**, *393*, 51–57.
- (93) Frisch, M. J.; Trucks, G. W.; Schlegel, H. B.; Scuseria, G. E.; Robb, M. A.; Cheeseman, J. R.; Scalmani, G.; Barone, V.; Mennucci, B.; Petersson, G. A.; et al. *Gaussian 09*, Revision B.01; Gaussian Inc.: Wallingford, CT, 2009.
- (94) Hehre, W. J.; Ditchfield, R.; Pople, J. A. Self-Consistent Molecular Orbital Methods. XII. Further Extensions of Gaussian-Type Basis Sets for Use in Molecular Orbital Studies of Organic Molecules. *J. Chem. Phys.* **1972**, *56*, 2257–2261.
- (95) Hoffmann, R. An Extended Hückel Theory. I. Hydrocarbons. *J. Chem. Phys.* **1963**, *39*, 1397–1412.
- (96) Mulliken, R. S. Electronic Population Analysis on LCAO-MO Molecular Wave Functions. I. *J. Chem. Phys.* **1955**, *23*, 1833.
- (97) Stuchebrukhov, A. A. Tunneling Currents in Electron Transfer Reaction in Proteins. II. Calculation of Electronic Superexchange Matrix Element and Tunneling Currents Using Nonorthogonal Basis Sets. *J. Chem. Phys.* **1996**, *105*, 10819.
- (98) Newton, M. D. Quantum Chemical Probes of Electron-Transfer Kinetics: The Nature of Donor-Acceptor Interactions. *Chem. Rev. (Washington, DC, U. S.)* **1991**, *91*, 767–792.
- (99) Katz, D. J.; Stuchebrukhov, A. A. New Expression for the Effective Transfer Matrix Element in Long-Range Electron Transfer Reactions. *J. Chem. Phys.* **1998**, *109*, 4960.
- (100) Daizadeh, I.; Gehlen, J. N.; Stuchebrukhov, A. A. Calculation of Electronic Tunneling Matrix Element in Proteins: Comparison of Exact and Approximate One-electron Methods for Ru-modified Azurin. *J. Chem. Phys.* **1997**, *106*, 5658.
- (101) Tan, M.-L.; Balabin, I.; Onuchic, J. N. Dynamics of Electron Transfer Pathways in Cytochrome C Oxidase. *Biophys. J.* **2004**, *86*, 1813–1819.
- (102) Skourtis, S. S.; Balabin, I. A.; Kawatsu, T.; Beratan, D. N. Protein Dynamics and Electron Transfer: Electronic Decoherence and Non-Condon Effects. *Proc. Natl. Acad. Sci. U. S. A.* **2005**, *102*, 3552–3557.
- (103) Medvedev, D. M.; Daizadeh, I.; Stuchebrukhov, A. A. Electron Transfer Tunneling Pathways in Bovine Heart Cytochrome C Oxidase. *J. Am. Chem. Soc.* **2000**, *122*, 6571–6582.
- (104) Lin, J.; Balabin, I. A.; Beratan, D. N. The Nature of Aqueous Tunneling Pathways between Electron-Transfer Proteins. *Science* **2005**, *310*, 1311–1313.
- (105) Antony, J.; Medvedev, D. M.; Stuchebrukhov, A. A. Theoretical Study of Electron Transfer between the Photolyase Catalytic Cofactor FADH[•] and DNA Thymine Dimer. *J. Am. Chem. Soc.* **2000**, *122*, 1057–1065.
- (106) Nishino, S.; Fujiwara, T.; Watanabe, N.; Yamamoto, S. Parameter Determination Procedure for Extended Hückel Approximation and Its Application for Solid-State Electrolytes. *J. Mol. Model.* **2015**, *21*, 1–13.
- (107) Inaba, T.; Tahara, S.; Nisikawa, N.; Kashiwagi, H.; Sato, F. All-Electron Density Functional Calculation on Insulin with Quasi-Canonical Localized Orbitals. *J. Comput. Chem.* **2005**, *26*, 987–993.
- (108) Olbrich, C.; Strümpfer, J.; Schulten, K.; Kleinekathöfer, U. Theory and Simulation of the Environmental Effects on FMO Electronic Transitions. *J. Phys. Chem. Lett.* **2011**, *2*, 1771–1776.
- (109) Pichierri, F. A Quantum Mechanical Analysis of the Light-Harvesting Complex 2 (Lh2) from Purple Photosynthetic Bacteria: Insights into the Electrostatic Effects of Transmembrane Helices. *BioSystems* **2011**, *103*, 132–137.
- (110) Ramos, P.; Pavanello, M. Quantifying Environmental Effects on the Decay of Hole Transfer Couplings in Biosystems. *J. Chem. Theory Comput.* **2014**, *10*, 2546–2556.
- (111) Roothaan, C. New Developments in Molecular Orbital Theory. *Rev. Mod. Phys.* **1951**, *23*, 69–89.